

# The study of topside ionospheric irregularities during geomagnetic storms in 2015

Oluwaseyi Jimoh<sup>1,2</sup> , Jiuhou Lei<sup>1,3,4,\*</sup>, Fuqing Huang<sup>1,3,4</sup> , and Jiahao Zhong<sup>5</sup>

<sup>1</sup> CAS Key Laboratory of Geospace Environment, School of Earth and Space Sciences, University of Science and Technology of China, Hefei 23000, China

<sup>2</sup> Department of Physics, Adeleke University, Ede 232101, Osun, Nigeria

<sup>3</sup> Mengcheng National Geophysical Observatory, University of Science and Technology of China, Hefei 230000, China

<sup>4</sup> CAS Center for Excellence in Comparative Planetology, University of Science and Technology of China, Hefei 230000, China

<sup>5</sup> School of Atmospheric Sciences, Sun Yat-Sen University, Zhuhai 519000, China

Received 8 September 2021 / Accepted 11 August 2022

**Abstract**—In this study, the variations of topside ionospheric irregularities during 24 geomagnetic storms with  $Dst \leq -50$  nT in 2015 were examined through an algorithm specifically designed to detect a significant level of ionospheric irregularities. The algorithm was developed through the use of several parameters derived from the topside total electron content (TEC) observations from GRACE, Swarm-C, and Swarm-B. The local time characteristics of the observed equatorial plasma irregularities (EPIs) were analyzed during different phases of the storms, within  $30^\circ$  S– $30^\circ$  N magnetic latitudes. By comparing its results with corresponding in-situ electron density data and the results of previous studies, the algorithm was found to be efficient. It was observed that the detected EPIs at different stages of the storm showed local time dependence. For instance, EPIs were observed during nighttime, but took place in the daytime occasionally during the storm main phase. Furthermore, the percentage occurrence rates were most prominent during the main phase at the post-sunset sector within less than 6 h of the storm onset. On the other hand, the occurrence rates became prominent in the post-midnight/morning sector during the recovery phase and even higher than observed in the post-sunset sector. Based on these findings it was concluded that the dominant driver of the enhanced EPIs during the post-midnight/daytime sector could be associated with disturbance dynamo electric fields.

**Keywords:** Topside ionosphere / Equatorial plasma irregularities / Geomagnetic storm / Rate of total electron content index (ROTI) / Disturbance dynamo electric fields

## 1 Introduction

Ionospheric irregularities refer to the existence of plasma inhomogeneities in the ionosphere, which spans a large range of scale sizes, from hundred-kilometers down to the sub-kilometer range, and exists at all latitudes. Particularly, the occurrence of irregularities at the equatorial and low latitudes has a special type of feature called equatorial plasma bubbles (EPBs), which is marked by large-scale depletion in electron density usually accompanied by smaller scale irregularities. The equatorial plasma irregularities (EPIs) associated with EPBs are a common nighttime phenomenon that has a consequential effect on the performance of radio communication and navigation. They are known to commence below and above the *F*-layer peak at about 19:00 LT and 20:00 LT, respectively (Kil & Heelis, 1998).

The topside ionospheric irregularities during the post-sunset sector are triggered from the bottom side as magnetic field-aligned plasma depletions or what is generally referred to as EPBs, which drift upward with a speed of  $\sim 150$  ms<sup>-1</sup> (McClure et al., 1977). The characteristics of EPIs during quiet and disturbed times and the mechanism by which they are generated have been well established. The Rayleigh–Taylor instability (RTI) mechanism during the post-sunset period has been credited to the occurrence of *F*-region plasma irregularities in the equatorial/low-latitude region (Sultan, 1996; Kelley, 2009; Abdu, 2019). These EPIs are initiated at the bottom side *F* region and the nighttime polarization electric fields play an important role in the non-linear growth of these EPIs from the bottom-side and their appearance at the topside.

The background zonal electric fields play a vital role in the development of EPIs and may act to enhance (inhibit) the mechanism responsible for irregularity occurrence if it is in the eastward (westward) direction (Stolle et al., 2008; Su et al., 2008).

\*Corresponding author: [leijh@ustc.edu.cn](mailto:leijh@ustc.edu.cn)

The  $E \times B$  drift at the equator is known to significantly increase and reverse in polarity near the sunset terminator, and it is referred to as pre-reversal enhancement (PRE) (Rishbeth, 1971; Eccles et al., 2015). It has been observed that at nighttime, the  $E$  region plasma density becomes washed out as a result of chemical recombination and thereby loses its ability to short out the electric field that is being produced by the  $F$ -region dynamo. The combination of the rapid rise of the  $F$ -layer and the bottom side steep vertical density gradient at the equatorial region gives rise to the Rayleigh–Taylor instability condition in the nighttime background ionosphere and predisposes it to the occurrence of plasma irregularities. Other parameters such as upward propagating gravity waves (Rottger, 1981; Tsunoda, 2010; Li et al., 2016), collisional shear instability (Hysell & Kudeki, 2004), and meridional wind component (Maruyama, 1988; Abdu et al., 2006; Su et al., 2018) have also been associated with the conditions necessary for the RTI. Hence, the generalized RTI growth rate ( $\gamma$ ) which incorporates all concerned parameters is given by the following equation (Sultan, 1996):

$$\gamma = \frac{\sum_P^F}{\sum_P^E + \sum_P^F} \left( V_{\text{dr}} - U_{\perp} - \frac{g}{v_{\text{in}}^{\text{eff}}} \right) \frac{1}{L_n} - R_T \quad (1)$$

where  $g$  is the acceleration due to gravity,  $v_{\text{in}}^{\text{eff}}$  is the flux tube-integrated effective  $F$  region ion-neutral collision frequency weighted by number density along the flux tube,  $V_{\text{dr}}$  is the  $E \times B$  vertical plasma drift component,  $U_{\perp}$  is the Pedersen conductivity weighted flux tube-integrated neutral wind that is perpendicular to the magnetic field line,  $L_n$  is the scale length of the vertical gradient of the flux tube-integrated plasma density measured at the equator,  $R_T$  is the flux tube-integrated recombination rate (Basu, 1997),  $\sum_P^E$  and  $\sum_P^F$  are the integrated Pedersen conductivities in the  $E$  and  $F$  regions, respectively.

The  $V_{\text{dr}}$  parameter in equation (1), which also represents the PRE, has been the most widely discussed contributor to the RTI growth rate and can get modified during geomagnetic storms by prompt penetration of magnetospheric electric field and disturbance dynamo electric field (Heelis et al., 1974; Farley et al., 1986; Eccles et al., 2015; Abdu, 2019). During geomagnetic storm and under southward incursion of  $B_z$ , interplanetary electric field maps to the high latitudes as dusk-dawn electric field and penetrates to the low-latitude as under-shielding prompt penetration electric field (PPEF) having eastward (westward) orientation on the dayside (night-side) and manifests usually during the main phase. When the  $B_z$  turns northward an over-shielding electric field penetrates to the low-latitude having an opposite polarity to the under-shielding PPEF (Kikuchi et al., 2000). Similar to the over-shielding PPEF is the disturbance dynamo electric field (DDEF) that arises from the equatorward thermospheric disturbance wind due to storm-time auroral heating mostly during the recovery phase of a geomagnetic storm (Blanc & Richmond, 1980; Richmond et al., 2003). The superposition of the vertical drift by under-shielding PPEF during the daytime/evening (post-midnight/pre-sunrise) hours can cause rapid uplift (descent) of the  $F$  layer, while the reverse is the case for both over-shielding PPEF and DDEF (Abdu et al., 2003; Abdu, 2012).

The ionospheric irregularities that occur during the post-midnight/post-sunrise have been positively correlated with geomagnetic activity (Fejer et al., 1976; Aarons & DasGupta, 1984;

Zakharenkova et al., 2015; Luo et al., 2020). During the post-midnight/pre-sunrise and quiet geomagnetic condition, the zonal electric field has a westward direction and causes a downward drift of plasma via the  $E \times B$  effect in the equatorial region. Hence, EPI may occur during the post-midnight local times provided there is a reverse in the quiet time zonal electric field direction (Fejer et al., 1976; Bowmann, 1978; Burke, 1979). From previous literature, it is known that the occurrence of a geomagnetic storm is one of the possible ways by which the electric fields' direction can be reversed (Fejer & Scherliess, 1995; Abdu, 2016). The reversal of the quiet time zonal electric field component from westward to eastward will raise the  $F_2$  peak height. Besides, Wan et al. (2019) have also shown that the irregularities that are observed during predawn sector under geomagnetic disturbed conditions are predominantly due to fossil EPIs of the previous nighttime and possibly strengthened by upward drift of plasma due to PPEF. Occurrence of daytime plasma irregularities have also been occasionally observed to be associated with rocket exhaust (Park et al., 2016; Li et al., 2018).

The EPI phenomenon has been extensively studied using several instruments such as ionosondes (Booker & Wells, 1938; Abdu et al., 1981), coherent and incoherent scatter radars (Woodman & La Hoz, 1976; Greenwald et al., 1995; Hysell & Burcham, 1998; Jin et al., 2018), airglow imagers (Makela & Miller, 2008); VHF/UHF and Global Navigation Satellite Systems (GNSS) receivers (Basu et al., 2001; Seemala & Valadares, 2011; Sun et al., 2012; Zakharenkova & Astafyeva, 2015; Amaechi et al., 2020) and in situ satellite probes (McClure et al., 1998; Xiong et al., 2010; Huang et al., 2014). The global coverage of GNSS receivers has made the investigation of ionospheric irregularities much easier and convenient through the use of the rate of total electron content (TEC) index (ROTI), which is a proxy for scintillation indices that are derived from the rather scarce scintillation monitors (Pi et al., 1997; Oladipo & Schüler, 2013; Zakharenkova & Astafyeva, 2015; Bolaji et al., 2018; Li et al., 2020).

The application of ROTI can also fill the gap in the topside ionospheric investigation when/where in situ electron density (Ne) data are not available. More importantly, it has also been realized that the topside ROTI technique can probe ionospheric irregularities ahead/behind/aside low Earth orbit (LEO) position and for a much longer time than in situ cross-section (Zakharenkova et al., 2015). The ROTI is, without doubt, a very useful index in characterizing ionospheric irregularities, but due to the nature of its absolute value, it cannot distinguish between plasma depletions and enhancements. Furthermore, the use of ROTI derived from topside TEC in investigating ionospheric irregularities is not quite straightforward as it is with the one derived from ground-based TEC data.

This complexity can be attributed to a number of factors such as; relative motion between the GNSS receiver and the plasma structures. The topside ROTI tends to contain a combination of the drifting structures/irregularities and stationary ionospheric gradients such as equatorial ionosphere anomaly (EIA). Furthermore, there is also the issue of the limited time of individual GNSS tracking by the LEO satellite, hence the TEC profile from a single GPS arc can only provide a portion of the single orbit profile that the in-situ electron density data can provide. Although some studies on ROTI derived from topside TEC have been carried out previously

**Table 1.** The orbital characteristics of the satellites and the onboard instruments.

Satellite	Mean altitude (km)	Orbital period (min)	TEC sampling rate (Hz)	Ne sampling rate (Hz)	Orbit
GRACE	395	94.5	1/10	1	Polar
SWC	460	96	1	2	Polar
SWB	515	96	1	2	Polar

(Zakharenkova et al., 2015, 2016; Cherniak & Zakharenkova, 2016; Jimoh et al., 2019; Jin et al., 2019), only Zakharenkova et al. (2016) had attempted to address the challenge of the density gradient due to the EIA structures appearing as enhancements in the ROTI derived from topside TEC, although it was not explicitly dealt with. For instance, the authors did not disclose the length of the multiple peaks that they used. This implies that no study has paid keen attention to resolving the challenges that abound when applying the ROTI technique to the investigation of topside ionospheric irregularities.

Several case and statistical studies have been carried out on the morphology of ionospheric irregularities during geomagnetic storms (Oya et al., 1986; Watanabe & Oya, 1986; Abdu, 1997; Li et al., 2010; Abdu, 2012; Sun et al., 2012; Huang et al., 2013; Zakharenkova et al., 2015; Li et al., 2018; Jimoh et al., 2019; Huang et al., 2021). Most of the previous statistical studies on ionospheric irregularities during geomagnetic storms were not focused on the post-midnight to the pre-noon sector while a few of those focused on the post-midnight to the post-sunrise sector did not use the topside ROTI technique in detecting irregularities (Burke, 1979; Greenspan et al., 1991; Huang et al., 2001; Wan et al., 2019; Aa et al., 2020). Hence, this study is based on the detection of a significant level of equatorial plasma irregularities during 24 geomagnetic storm events in 2015 by the means of an algorithm, which used the ROT/ROTI derived from three LEO satellites' topside TEC observations, both during the daytime and nighttime sectors.

This study has the following objectives: firstly, to resolve the challenges associated with applying the ROTI derived from topside TEC data in detecting irregularities, secondly, to study the occurrence characteristics of the topside ionospheric irregularities during geomagnetic storms ( $Dst < -50$  nT) in 2015 using the topside ROTI technique.

## 2 Methodology

### 2.1 Instrument and data

Multi-instrument datasets were used in this study and they include the topside TEC retrieved from GPS receivers aboard Gravity Recovery and Climate Experiment (GRACE), Swarm-C (SWC), and Swarm-B (SWB), the in situ electron density (Ne) retrieved from the Swarm's Langmuir probes and GRACE's K-Band ranging system (Tapley et al., 2004; Choi & Lightsey, 2008; Friis-Christensen et al., 2006; Lei et al., 2014), and the rate of TEC index (ROTI) derived from the topside TEC. The orbital characteristics of the satellites and the sampling rates of the GPS receivers and of the electron density detectors are given in Table 1. It should be noted that in this study only the GPS satellites were tracked. The topside TEC as used here refers to the TEC measurements that are obtained above the orbital altitude of the aforementioned LEO

satellites from their onboard dual-frequency GPS observables. The relative slant TEC between the GPS receivers at the orbital heights of the LEO satellites and GPS satellites is derived by first eliminating the outliers, using the well-known technique proposed by Blewitt (1990) to detect and correct cycle slips, and the pseudorange TEC is used to adjust the level of the carrier phase TEC per phase-connected arc (Mannucci et al., 1998).

Furthermore, the absolute slant TEC was retrieved after removing the inter-frequency biases. The GPS satellites' biases can be obtained from the international Global Navigation Satellite Systems Service and the receivers' biases were estimated via the least square algorithm (Yue et al., 2011; Zhong et al., 2016a,b). A geometric mapping function (Foelsche & Kirchengast, 2002) was used to convert the slant TEC to vertical TEC ( $vTEC$ ), and the ionospheric effective height was selected as a function of the orbital altitude of the LEO satellite and solar activity (Zhong et al., 2016c). In order to minimize the error caused during the conversion of slant TEC to vertical TEC, a cutoff elevation angle of  $30^\circ$  was used in this study.

The ROTI derived between the GPS to any LEO satellite's link is a parameter used in describing the topside ionospheric irregularity condition and can be computed by taking the following steps. Firstly, calculating the rate of TEC (ROT) by taking the ratio of the difference between two consecutive epochs of vertical TEC to the time interval in units of TECU/min,  $1 \text{ TECU} = 10^{16} \text{ el/m}^2$  (Pi et al., 1997). Note that only  $vTEC$  data that had a data length of at least 4 min were considered in the computation of ROT

$$\text{ROT} = \frac{v\text{TEC}_k^i - v\text{TEC}_{k-1}^i}{t_k - t_{k-1}} \quad (2)$$

where  $i$  is the GPS satellite in view of the LEO satellite and  $k$  is the time of epoch. Secondly, the ROTI is then computed by taking the running standard deviation of ROT with a 1-min window as given below;

$$\text{ROTI} = \sqrt{\langle \text{ROT}^2 \rangle - \langle \text{ROT} \rangle^2} \quad (3)$$

A similar approach was also adopted to obtain the rate of density index (RODI), from the in-situ electron density. RODI is also a good measure of ionospheric irregularities, which has been proven to be consistent with ROTI technique in the detection of irregularities (Zakharenkova & Astafyeva, 2015; Jimoh et al., 2019). RODI was used for the purpose of comparison with ROTI.

### 2.2 Algorithm description

In order to overcome the challenges associated with the application of topside ROTI to EPI study as earlier mentioned, a suitable technique different from the approach of

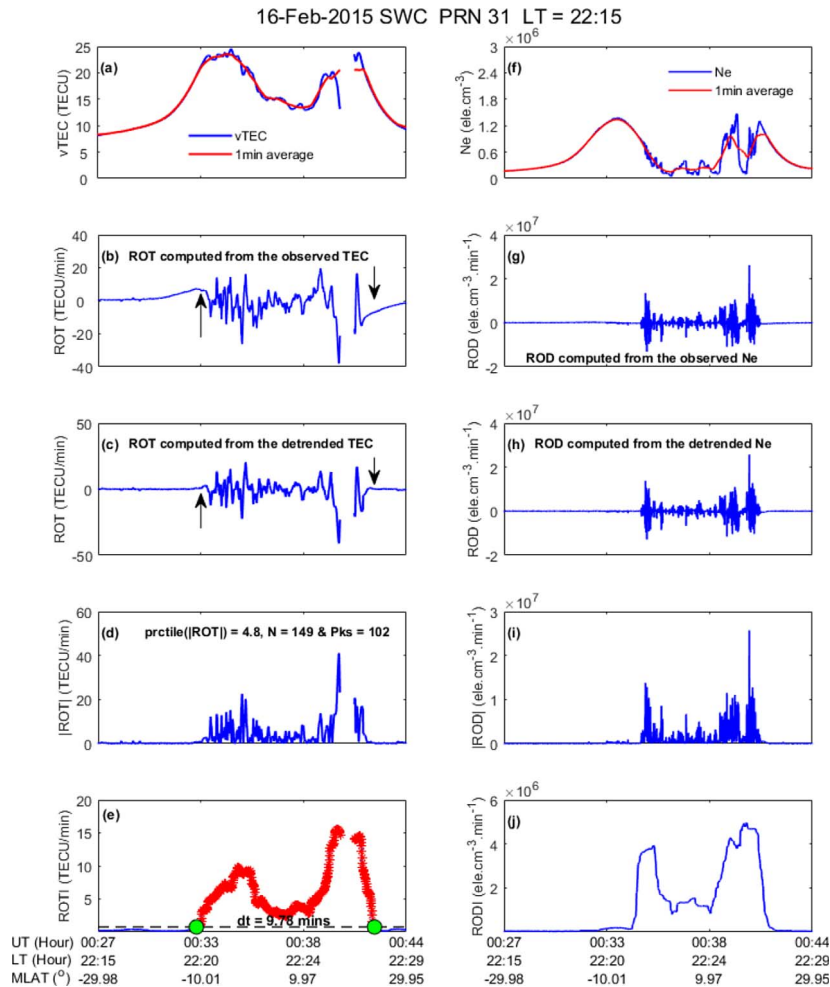


**Fig. 1.** An example illustrating the occurrence of ionospheric irregularities on 16 February 2015 observed by Swarm-C along the line of sight of GPS PRN 31 around 22:14 LT. (a) and (f) The observed (blue) and the 1-min running average (red) vTEC and Ne data, respectively. (b) and (g) The rate of TEC (ROT) and rate of Ne (ROD) obtained from the observed vTEC and Ne, respectively. (c) and (h) ROT and ROD obtained from the detrended TEC and Ne, respectively. (d) and (i) The absolute values of detrended ROT and ROD, and (e) and (j) the values of the rate of TEC index (ROTI) and rate of Ne index (RODI). The  $\text{prctile}(|\text{ROT}|)$  in Figure 1d refers to the value of the 25th and 75th inter-percentile range of the detrended  $|\text{ROT}|$  when  $\text{ROTI} \geq 0.75$  TECU/min,  $N$  is the corresponding data population and  $\text{Pks}$  is the number of peaks (local maxima) in  $|\text{ROT}|$  when  $\text{ROTI} \geq 0.75$  TECU/min. The horizontal dashed black line indicates  $\text{ROTI} = 0.75$  TECU/min, and  $dt$  is the time interval (the start and end indicated by the two green solid circle) when  $\text{ROTI} \geq 0.75$  TECU/min (red).

Zakharenkova et al. (2016), with a longer time interval of 60 s for the computation of ROTI was developed to eliminate undesirable enhancements in ROTI.

In this study, the EPIs due to storm effects were of interest and as a result, the conditions were set so as to detect a significant level of irregularities both in the daytime and nighttime sectors. The latitudinal coverage was limited to  $30^\circ$  S– $30^\circ$  N magnetic latitudes due to the peculiarities that exist in different regions. In Figures 1–4 some cases were presented to serve as precedence to the conditions that were set in the algorithm for the detection of irregularities. In Figures 1–4, panels (a)–(e) show the vTEC (the raw and 1-min running average TEC), rate of TEC (ROT) computed from the raw TEC, ROT computed from the detrended TEC using 1-min running average, the absolute value of the detrended ROT ( $|\text{ROT}|$ ) and the ROTI computed from the detrended ROT, respectively, while

(f)–(j) represents the corresponding Ne and similar derivatives as done in (a)–(e) for TEC. The horizontal black dashed line and red curve indicate ROTI equal to and greater than 0.75 TECU/min, respectively, while the green solid circles indicate the start and end of the time interval ( $dt$ ) of  $\text{ROTI} > 0.75$  TECU/min. The horizontal axes of these figures show the universal time (UT), local time (LT) and magnetic latitude (MLAT).

Figure 1 shows an event on 16 February 2015 observed by SWC during 00:26–00:45 UT along the line of sight of GPS PRN 31. In Figure 1a and f, both TEC and Ne observations indicate plasma depletion-like feature between 00:32 and 00:42 UT during 22:14 LT. The feature is such that part of the Ne depletion in Figure 1f caused a corresponding disruption in the GPS radio signal shown by the gap in the TEC data in Figure 1a, which is an indication of ionospheric irregularities

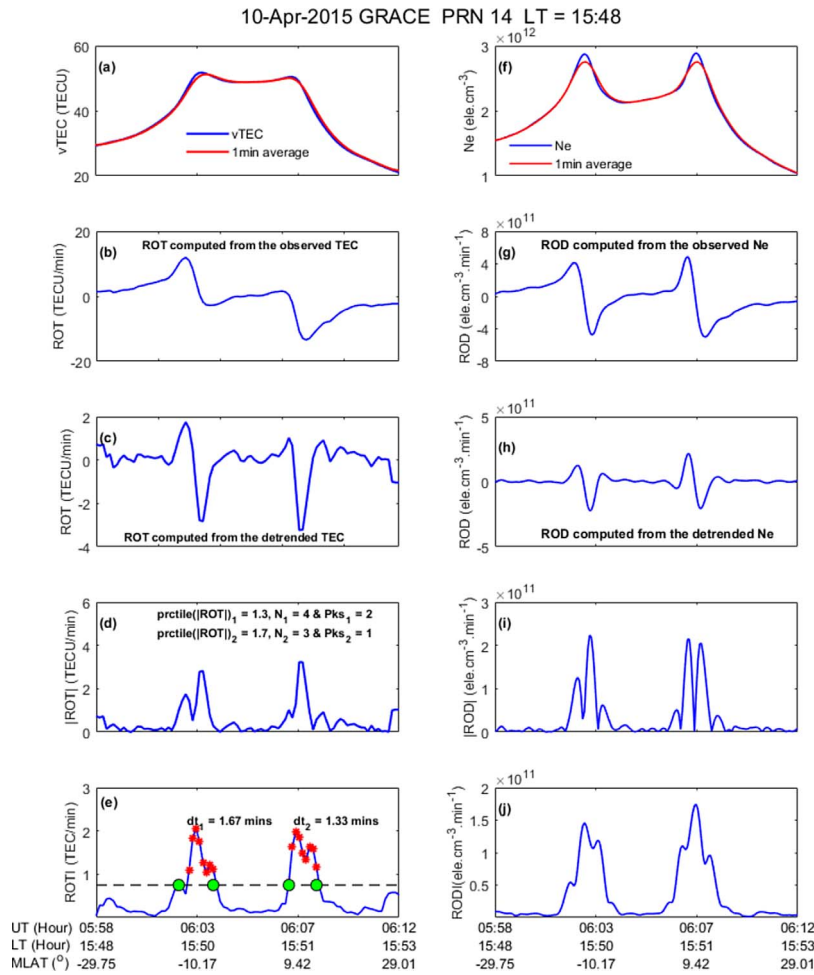


**Fig. 2.** An example of the TEC/Ne gradient (non-spread F) due to the equatorial ionospheric anomaly (EIA) was observed on 10 April 2015 by GRACE around 15:47 LT. The figure format is similar to the descriptions in Figure 1.

due to equatorial plasma bubbles. Furthermore, the irregularities were also revealed in the variations of ROT/ROTI in the subsequent sub-figures. Figure 1b shows some trends in the computed ROT from raw TEC, but the trend could not be observed in Figure 1c owing to the 1-min running average detrend of the TEC data (see the inset black arrows).

On the other hand, there was no notable difference between the ROD that was derived from the observed and detrended Ne in Figure 1g and h, respectively. Figure 1d shows the absolute value of the detrended ROT in Figure 1c. The number of peaks (local maxima) of  $|\text{ROT}|$  during the interval that ROTI was equal to and above a certain threshold (0.75 TECU/min) was found to be 108 (i.e.  $\text{Pks} = 108$ ), while the corresponding 25th and 75th inter-percentile range data population ( $N$ ) and value (prctile) of  $|\text{ROT}|$  during the interval  $\text{ROTI} \geq 0.75$  TECU/min are 163 and 2.9 TECU/min, respectively. In Figure 1e the ROTI was below 0.75 TECU/min until 00:32 UT and above this value for about  $dt = 9.78$  min. Generally, the characteristics of the irregularities observed in Figure 1f–j by the Ne and its derivatives show that the irregularity event is significant.

In Figure 2 a non-spread F but enhanced ROTI case as observed by GRACE along the line of sight to GPS PRN

14 on 10 April 2015 during 05:55–06:15 UT at 15:47 LT is shown. There are two conspicuous peaks in ROT/ROTI on both hemispheres of the magnetic equator, which indicates the presence of EIA in the ROT/ROTI observation. Such a case of enhanced ROTI has to be eliminated in the consideration of ionospheric irregularities. In addition, the TEC and Ne profiles in Figure 2a–c and f–h did not show significant fluctuations as the case shown in Figure 1. Furthermore, considering that the time interval between these peaks was more than a certain time limit (e.g. 2 min), the data points before and after this interval were considered independent events. However, it can be observed that the two events were not well populated with data, that is,  $N_1 = 4$ ,  $N_2 = 3$ , while the inter-percentile values of  $|\text{ROT}|_1 = 1.2$  TECU/min, and  $|\text{ROT}|_2 = 1.0$  TECU/min and the number of peaks  $\text{Pks}_1 = 2$  and  $\text{Pks}_2 = 1$  as shown in Figure 2d. Figure 2e shows that the  $\text{ROTI} \geq 0.75$  TECU/min during these events occurred within short durations,  $dt_1 = 1.67$  min and  $dt_2 = 1.33$  min and hence, these events and such like have to be systematically removed.

In Figure 3a and f, a case of spurious depletions in TEC and Ne from SWB observations during 11:48–12:07 UT on 7 November 2015 and around 01:03 LT is shown. Although this can be regarded as a valid EPI event, but for the purpose

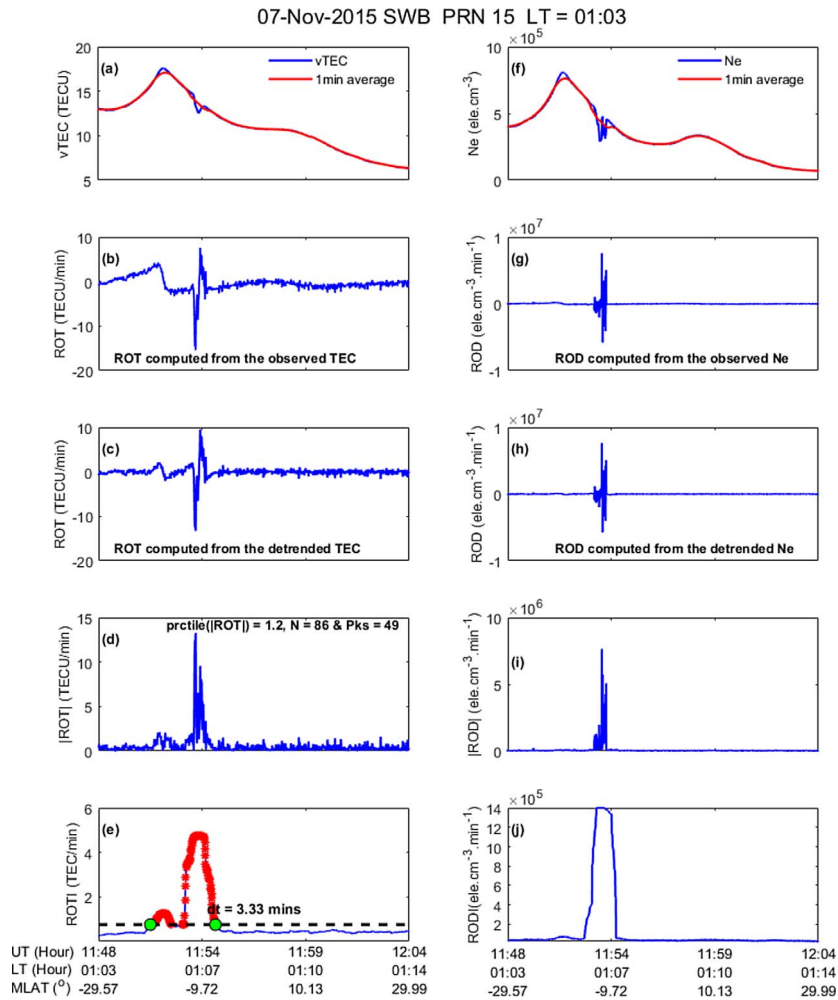


**Fig. 3.** Illustration of spurious depletion in TEC and Ne observed by Swarm-B on 7 November 2015. The figure format is similar to the descriptions in [Figure 1](#).

of this study it will not be considered as a significant event. The depletion was quite rapid and occurred in less than a minute as seen in [Figure 3a–d and f–i](#). In [Figure 3d](#),  $\text{prctile}(|\text{ROT}|) = 1.2$  TECU/min,  $N = 86$  and  $\text{Pks} = 49$  and  $dt = 3.33$  min ([Fig. 3e](#)). The interval of the  $\text{ROTI} \geq 0.75$  TECU/min does not indicate significant level of fluctuations. Hence, this case and other similar ones were not considered by this technique.

Daytime plasma density irregularities are generally unusual, except during special phenomena such as geomagnetic storms. An example of daytime plasma irregularities that occurred on 02 March 2015 at 10:31 LT observed by SWB along the GPS PRN 4 is shown in [Figure 4](#). The features of the TEC and Ne profiles shown in [Figure 4a and f](#), respectively did not show the usually pronounced Ne depletion common to the nighttime EPIs. The other sub-figures showed that the fluctuations in the radio signal ([Fig. 4c–e](#)) is quite pronounced owing to the irregular structures that characterized the in-situ plasma density ([Fig. 4f–j](#)). Based on these examples and further analysis, the following steps outline the basic conditions used to develop the algorithm:

Firstly, the topside TEC data from a LEO satellite to any GPS satellite that are tracked for at least 4 min were detrended using 1-min centered running average. This helps to remove the trend in the TEC data before computing the ROT.

Secondly, the ROTI was computed and a threshold 0.75 TECU/min that lasted for at least 2 min was set for the detection of irregularities. In addition, any two events that are separated by less than 2 min were merged as one event.

Thirdly, the number of peaks (local maxima) in  $|\text{ROT}|$  during the interval that  $\text{ROTI} \geq 0.75$  TECU/min should be at least 1-min length of data for high rate GPS receivers (Swarm) and at least 2 min length of data for lower rate GPS receivers (GRACE). This helps to eliminate the EIA and other non-EPI large-scale structures.

Fourthly, to ascertain the existence of irregularities during  $\text{ROTI} \geq 0.75$  TECU/min so as distinguish TEC depletion from enhancement a further step was taken. This was done by setting the data population ( $N$ ) and the value (prctile) of the 25th and 75th inter-percentile range of  $|\text{ROT}|$  to at least 2 min length of data and 1 TECU/min, respectively, within the interval of  $\text{ROTI} \geq 0.75$  TECU/min ([Pradipta et al., 2015](#)). These two

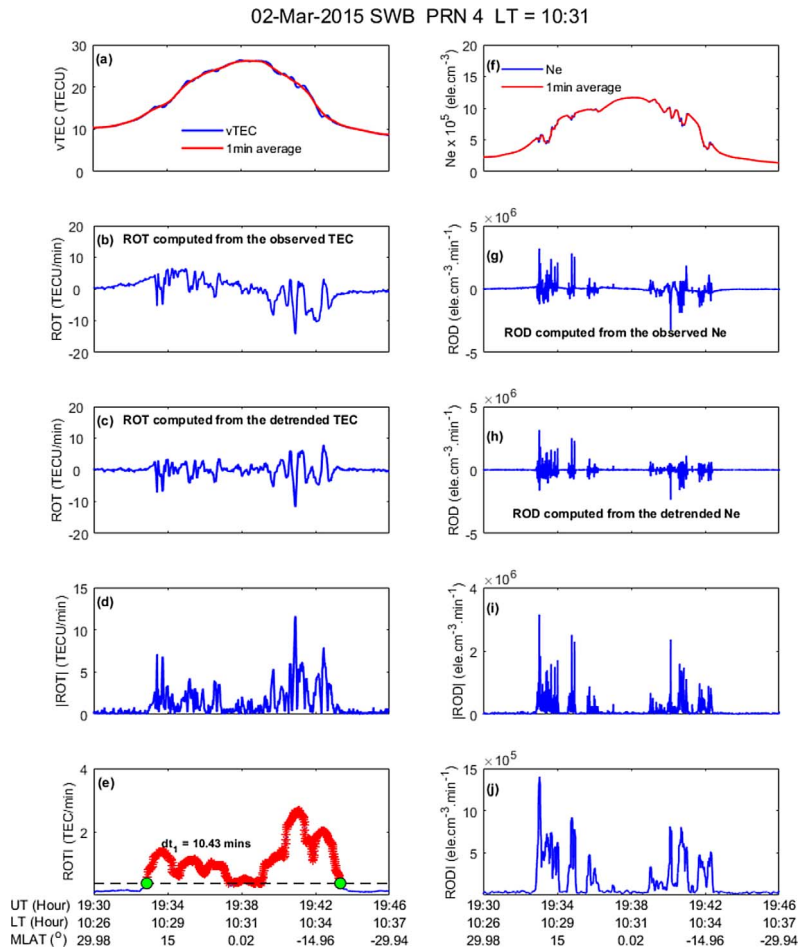


**Fig. 4.** A typical example of a daytime occurrence of ionospheric irregularities during the 02 March 2015 geomagnetic storm observed by Swarm-B along GPS PRN 4 at about 10:31 LT. The sub-figure descriptions are as given in Figure 1.

parameters can also help to eliminate non-EPI-related events. Note that the choices of the thresholds highlighted above depend on the intensity of ionospheric irregularities that is of interest and the sampling rates of the GPS receivers.

This technique counts the occurrence of EPI events once per GPS arc. It is to be noted that this counting strategy has a limitation in the sense that the proximity of the irregularity structure to the LEO satellite will determine the magnitude of the ROTI that will be observed by the tracked GPS. Hence, the position of some GPS satellites with respect to the LEO satellite may be more favorable in observing the EPIs than others. Furthermore, the scale sizes of the EPIs that are of interest predefines the criteria set for the algorithm. This implies that there are certain valid EPIs that may not be accepted as significant EPIs by the algorithm and such is the case with Figure 3. However, this should not affect the outcome of this study quite much.

In order to validate this technique, the combined data of all the satellites from 01 November 2014 to 31 December 2015 are presented in Figure 5 to show the global distribution of the EPIs encountered during  $kp < 4$  for the four-month season namely: (a) combined equinoxes, (b) June solstice, and (c) December solstice. The data were binned into  $2^\circ \times 5^\circ$  resolution in geographical latitude and longitude, and a local time range of 18–06 h while the gray line shows the dip equator. In each

bin, the occurrence rate of EPI is calculated as the ratio of the number of the GPS arcs that detected EPI events to the total number of tracked GPS arcs.

The result, as shown in Figure 5 is consistent with Zakharenkova et al. (2016) who used Swarm data during the same period in their study. The occurrence rate is high around the Atlantic Ocean during the combined equinoxes, maximizes around the Brazil-Atlantic Ocean during the December solstice, and maximizes at the African sector during the June solstice. The seasonal-longitudinal variation of the EPI occurrence also agrees with previous works (Burke et al., 2004; Yizengaw & Groves, 2018; Wan et al., 2018; Park et al., 2021) and it proves that the technique developed in this study is suitable for further analysis.

### 2.3 Geomagnetic storm phases criteria

Geomagnetic storms with  $Dst \leq -50$  nT in the year 2015 were selected, although not all storms with  $Dst < -50$  nT were considered due to certain constraints (e.g. multiple occurrences of the main phase within a short time). In the analysis, the data of four days during each storm event were analyzed spanning from the day of the initial phase onset to the day of the recovery phase.

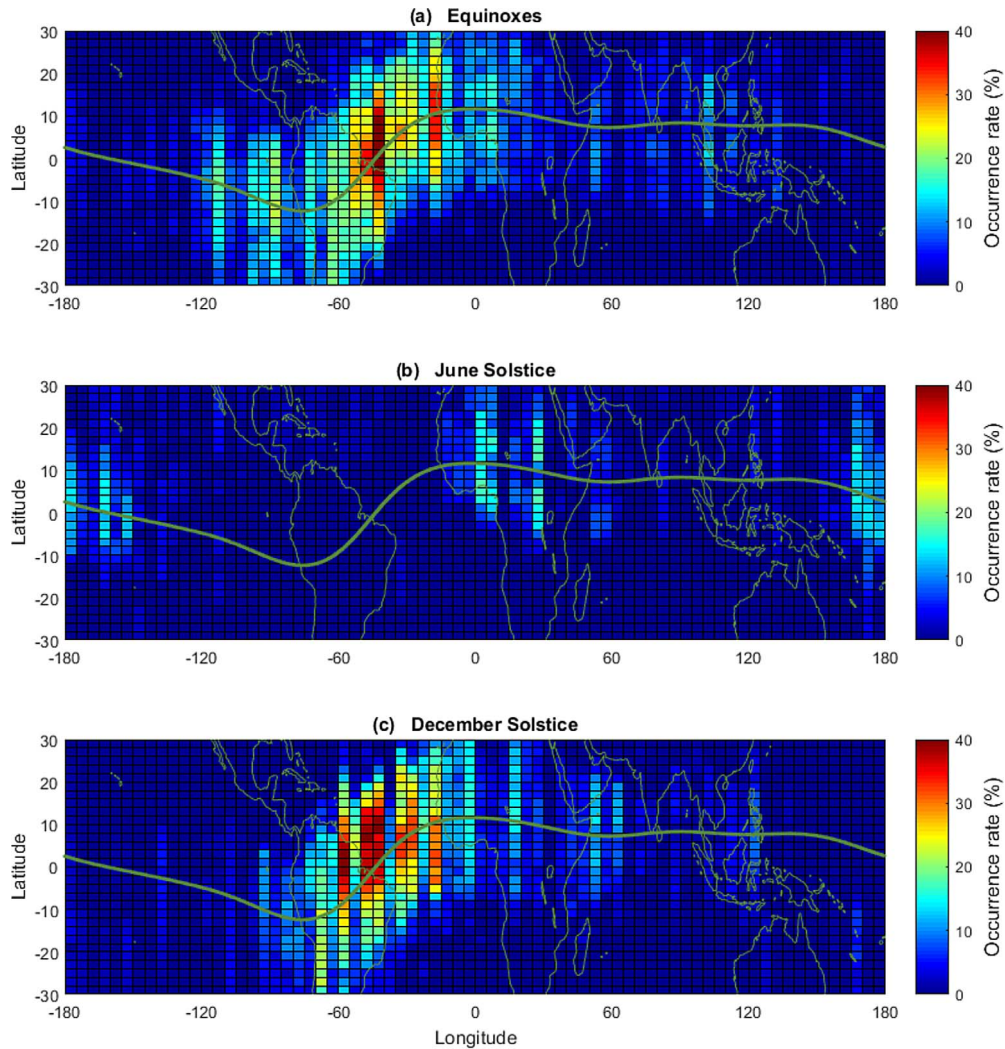


**Fig. 5.** The occurrence rate of the equatorial plasma irregularities of all the combined satellites from 01 November 2014 to 31 December 2015 under  $kp < 4$ : (a) combined equinoxes (b) June solstice (c) December solstices. The gray curve represents the dip equator.

The criteria for the selection of the storm phases were similar to those of [Walach & Grocott \(2019\)](#) but with slight modifications. The SYM-H index was used to categorize the storms' phases. The beginning of the initial phase was identified using the sudden storm commencement (SSC, <http://isgi.unistra.fr/>). The SSC usually indicates the variations of the Earth's magnetic field due to the Chapman–Ferraro current. However, manual selection of a relatively quiet time based on the conditions of Bz, AE and SYM-H was done occasionally to determine the beginning of the initial phase for the storms without SSC. The main phase onset was identified by the last point where SYM-H crossed the  $-30$  nT prior to the minimum SYM-H. The end of the main phase and beginning of the recovery phase, which are the same were chosen as the point when the SYM-H reached its minimum level. The end of the recovery phase was chosen as the time when SYM-H reached the quiet level ( $-15$  nT) thereafter ([Walach & Grocott, 2019](#)). However, manual check was done to select this phase whenever this condition was not satisfied after two days from the day of the minimum SYM-H. The summary of the dates of the storms' phases is presented in [Table 2](#).

### 3 Results

[Figure 6](#) shows the peak values of the time of the minimum Dst, minimum Bz, peak AE, minimum Dst, and minimum value of the rate of change of Dst during each of the analyzed geomagnetic storms from the top to the bottom, respectively, and the  $Dst < -100$  nT are shown in black color. The peak values were shown here so as to present the intensity of each geomagnetic storm, as storm impact is usually most profound around the minimum Dst. The Dst rate was also shown since it is a sensitive proxy for monitoring the presence of penetration electric fields, and its peak value indicates the peak of the ring current intensification. Nearly, 50% of the events' minimum Dst occurred within 06:00–18:00 UT, 25% of the events were between 18:00 and 24:00 UT, while the rest fall between 00:00 and 06:00 UT. The stronger storms attained the minimum Dst between 20:00 and 24:00 UT with the exception of 23 June 2015 event that occurred near 06:00 UT. The minimum Bz of the storms were mostly below  $-10$  nT and the AE peaks were mostly above 1000 nT. The values of the Dst rate with time were generally below  $-10$  nT/h for more than 2 h, which is

**Table 2.** The dates and times of the selected geomagnetic storms' phases in 2015.

Initial phase onset	Main phase onset	Minimum Sym-H (nT)	End of recovery phase
2015-Jan-07 06:16	2015-Jan-07 08:28	-135	2015-Jan-09 17:09
2015-Feb-16 20:04	2015-Feb-17 21:25	-70	2015-Feb-18 21:04
2015-Feb-23 20:09	2015-Feb-24 01:57	-76	2015-Feb-24 21:23
2015-Mar-01 18:11	2015-Mar-02 06:16	-70	2015-Mar-03 04:11
2015-Mar-17 04:45	2015-Mar-17 07:53	-234	2015-Mar-19 16:22
2015-Apr-09 20:23	2015-Apr-10 02:33	-71	2015-Apr-10 12:40
2015-Apr-10 16:48	2015-Apr-10 22:08	-89	2015-Apr-12 11:51
2015-Apr-15 07:11	2015-Apr-15 15:50	-88	2015-Apr-18 07:37
2015-May-10 14:23	2015-May-11 00:59	-57	2015-May-11 23:34
2015-May-12 21:36	2015-May-13 05:12	-98	2015-May-14 23:22
2015-Jun-08 02:23	2015-Jun-08 06:55	-105	2015-Jun-09 13:07
2015-Jun-22 05:44	2015-Jun-22 19:21	-208	2015-Jun-24 13:25
2015-Jul-04 16:47	2015-Jul-04 21:11	-87	2015-Jul-07 19:49
2015-Jul-12 21:36	2015-Jul-13 04:05	-71	2015-Jul-14 16:27
2015-Jul-22 21:36	2015-Jul-23 05:06	-83	2015-Jul-24 11:42
2015-Aug-15 08:29	2015-Aug-15 11:44	-94	2015-Aug-18 13:52
2015-Sep-07 12:00	2015-Sep-07 17:44	-81	2015-Sep-08 09:38
2015-Sep-08 19:12	2015-Sep-09 01:32	-113	2015-Sep-10 15:44
2015-Sep-10 21:36	2015-Sep-11 08:00	-95	2015-Sep-13 05:50
2015-Sep-20 06:04	2015-Sep-20 06:56	-84	2015-Sep-21 10:18
2015-Oct-06 12:00	2015-Oct-07 04:13	-124	2015-Oct-09 07:41
2015-Nov-03 01:34	2015-Nov-04 05:41	-60	2015-Nov-04 19:40
2015-Nov-06 18:17	2015-Nov-07 01:59	-106	2015-Nov-08 11:10
2015-Dec-19 16:16	2015-Dec-20 06:16	-170	2015-Dec-22 23:05

below the 5 nT/h lasting for 2 h or more threshold used by Huang et al. (2002) for irregularities' occurrence.

Since EPIs are mostly dominant during the post-sunset and post-midnight sectors, the initial analysis was restricted to these sectors. Figure 7a–d and e–h shows the distributions of the numbers of observed EPI events (one count per GPS arc) and the percentage occurrences of EPI events, respectively. In each panel the upper segment represents the analysis done for the post-sunset while the lower segment represents the one for the post-midnight. The initial, main and recovery phases are represented with blue, green and yellow colors, respectively. Figure 7a–d shows that the number of observed irregularities is higher during the recovery phases and with greater proportion during the post-midnight sector.

However, because of the different orbital characteristics of the LEO satellites, the numbers of observed irregularities were weighted by the total numbers of observed GPS satellites in view of the LEO satellites during each phase and the results are presented in Figure 7e–h. The percentage occurrence was obtained by dividing the numbers of observed irregularities by the total number of GPS arcs tracked by the LEO satellite during an individual storm phase. These weighted occurrences show a higher percentage proportion during the main phase for the post-sunset sector, and during the recovery phase for the post-midnight sector. All the storms and the satellites were combined in subsequent results.

Figures 8–10 show the combined results of all the storms (from the initial phase onset to the end of the recovery phase) and satellites. Figure 8 shows the numbers of tracked GPS satellites with respect to local time during all the storms. This is useful before the investigation of LT dependence on EPIs. The green and dark blue colors represent the total numbers of GPS observed and the numbers of GPS that observed EPI

events, respectively. It can be observed that the EPIs mostly occur before 07:00 LT and after 18:00 LT, but some EPIs were also observed during 08:00–13:00 LTs. It can also be noticed that the lack of EPI events during 14:00–17:00 LT interval is not associated with the absence of GPS arcs.

Furthermore, the observation of higher numbers of EPIs during the 21:00–23:00 LT is not owned to higher numbers of GPS arcs or satellite orbital samples. Rather it can be observed that the relative numbers of the GPS arcs that observed storm time EPIs to the total numbers of observed GPS arcs during the storm period were highest in the post-sunset sector and followed by the post-midnight sector.

In Figure 9 the LT distributions of the storm time EPI are shown for all the combined seasons, equinoxes, June solstice, and December solstice in Figure 9a–d, respectively. The corresponding occurrence rates are shown in right panels. It should be noted that the storm period considered here was limited to the period between the main phase onset and the end of the recovery phase. The patterns of the storm time LT distribution of the numbers of observed EPIs show more consistence with the occurrence rate during the post-sunset sector, while a level of variation is noticed during the post-midnight and daytime sectors in Figure 9a and e.

It is also noteworthy from the result for the combined seasons in Figure 9a and b that the numbers of EPIs considerably reduced from 07:00 to 13:00 LT. The sudden increase in the numbers of EPIs at 10 LT may be associated with higher orbital sampling during this LT as shown in Figure 8. Moreover, it can also be noticed that the reason for no EPI at some LTs during some seasons is not related to the absence of GPS arcs during these seasons as shown in Figure 8.

Figure 10 shows the LT variations of the number of EPIs and occurrence rate during different epochs of the superposed

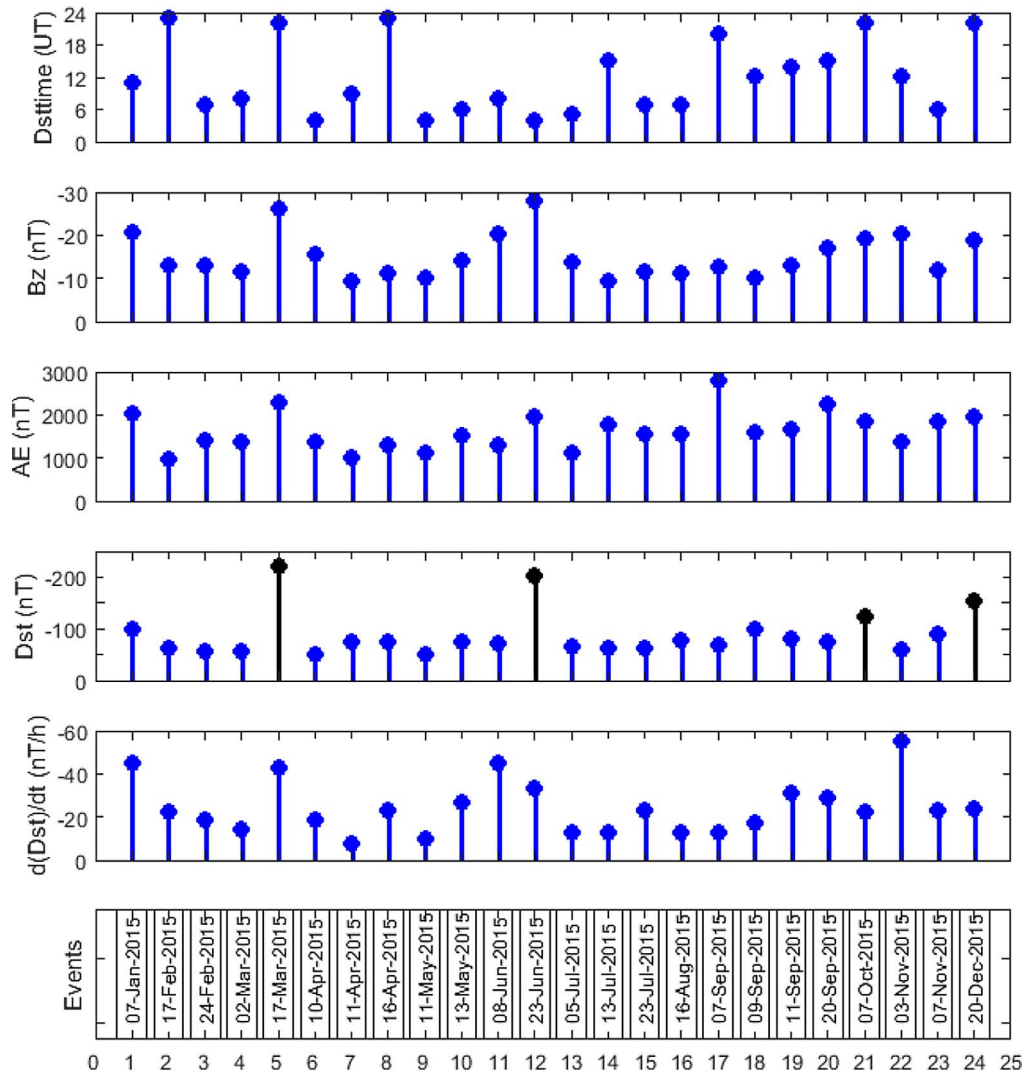


**Fig. 6.** The plot of the Dst minimum time (Dsttime), minimum southward interplanetary horizontal magnetic field (Bz), the peak value of auroral electrojet (AE), minimum Dst and the rate of Dst per hour (d(Dst)/dt) values during each storm event from top to bottom. The black lines indicate the storms with Dst < -100 nT.

storms. The numbers of EPIs were represented by the blue bars, and the occurrence rates are shown by the gray lines with labels on the left and right vertical-axes respectively. The main phase onset was set to 0 h and the stages of the superposed storms were divided into several epochs of 6 h width, 24 h prior to and 72 h after the 0 h as shown in Figure 10a–q. It can be observed in Figure 10a and b that EPIs only existed during 22:00–23:00 LT during the -3 and -4 epochs about 13 h or more prior to the first epoch. The EPI activities increase within 12 h prior to the first epoch at the post-sunset and also show eruptions of EPIs between the post-midnight and morning sectors.

During the 1st epoch, the EPI activities significantly increased by about double the previous epoch, and the EPIs got distributed to more LTs during the post-midnight sector. This indicates the impact of the storm forcing due to prompt penetration of electric fields (PPEF), which are active after the main phase onset and maximizes during the minimum SYM-H index. After 6 h from the storm onset (2nd epoch),

the EPI activities subsided during the post-sunset sector while it increased at the post-midnight/morning sectors with more LT coverage. This also indicates the effect of the delayed storm forcing in the form of disturbance dynamo electric fields (DDEF), which are more active several hours after the main phase onset during the recovery phase of geomagnetic storms.

The EPI activities got further subsided both in the post-sunset and post-midnight/morning sectors during the 3rd epoch, although enhancements and new EPI initiations can still be observed at some LTs between the post-midnight and noon sector (e.g. 06:00, 10:00, and 13:00 LTs). However, the EPI activities were more in the post-midnight/morning sector than in the post-sunset sector. This again supports the knowledge that the DDEF forcing is more active during the post-midnight sector after several hours into the storm (Bowmann, 1978; Burke, 1979; Huang et al., 2001; Wan et al., 2019). In Figure 10h during the 4th epoch the numbers of observed EPIs had significantly declined during the post-midnight but without significant change in the post-sunset. The decline of EPI

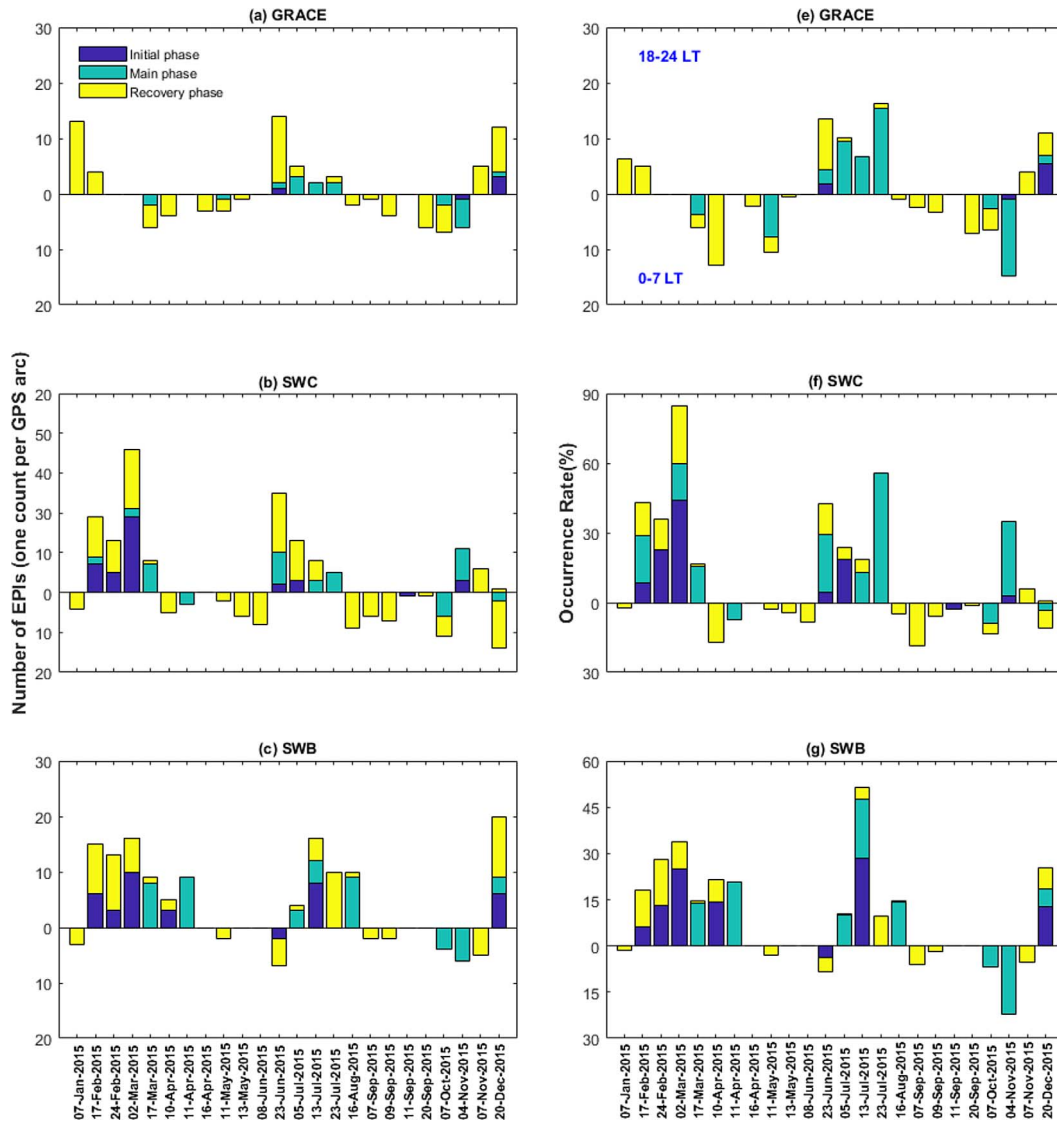


**Fig. 7.** The distribution of the number of observed irregularities during each storm phase (a)–(d) and the percentage of occurrences of irregularities (e)–(h) during each storm phase is calculated from the numbers of irregularities divided by the numbers of GPS arcs. The blue bars indicate the initial phase, green bars indicate the main phase and the yellow bars indicate the recovery phase. The upper segment of each panel (a)–(d) represents the distribution during post-sunset (18:00–24:00 LT) and the lower segment (e)–(h) during post-midnight (00:00–07:00 LT).

activities continued till the last epoch, with no EPI occurrence except during the 21:00 LT. The reason for near-total inhibition of EPIs during the epochs in [Figure 10m–q](#) may be due to the fact that only very few of the storms extended till the third day (see [Table 2](#)). The suppression of EPIs during the post-midnight in [Figure 10k–q](#) may imply that most of the storms fully recovered after 36 h from the main phase onset.

## 4 Discussion

This study presents the results of the systematic use of ROT/ROTI to infer ionospheric irregularities derived from the topside TEC aboard LEO satellites. The procedures of the technique used to effectively determine ionospheric irregularities at the topside at different altitudes and local times in the absence of

scintillation monitors and in situ electron density probes have been outlined. The criteria set for the detection of irregularities were dependent on the intensity of the irregularities that is of interest. Based on the orbital speed of  $\sim 7.6$  km/s and  $\sim 3.9$  km/s for the LEO and GPS satellites, respectively, the study specifically focused on EPIs of scales sizes between  $\sim 17$  km and  $\sim 500$  km for Swarm and between  $\sim 170$  km and  $\sim 500$  km for GRACE, which are relatively large scales of EPIs than studied by [Zakharenkova et al. \(2016\)](#). The technique was developed both to eliminate EIA structures and detect irregularities so as to discriminate between plasma depletions and enhancements, which are two major banes to the use of topside ROTI. Its limitations with respect to the counting strategy of the EPIs and the level of ‘significance’ accorded to the EPI event, which may lead to the exclusion of non-significant but valid EPIs have also been mentioned.

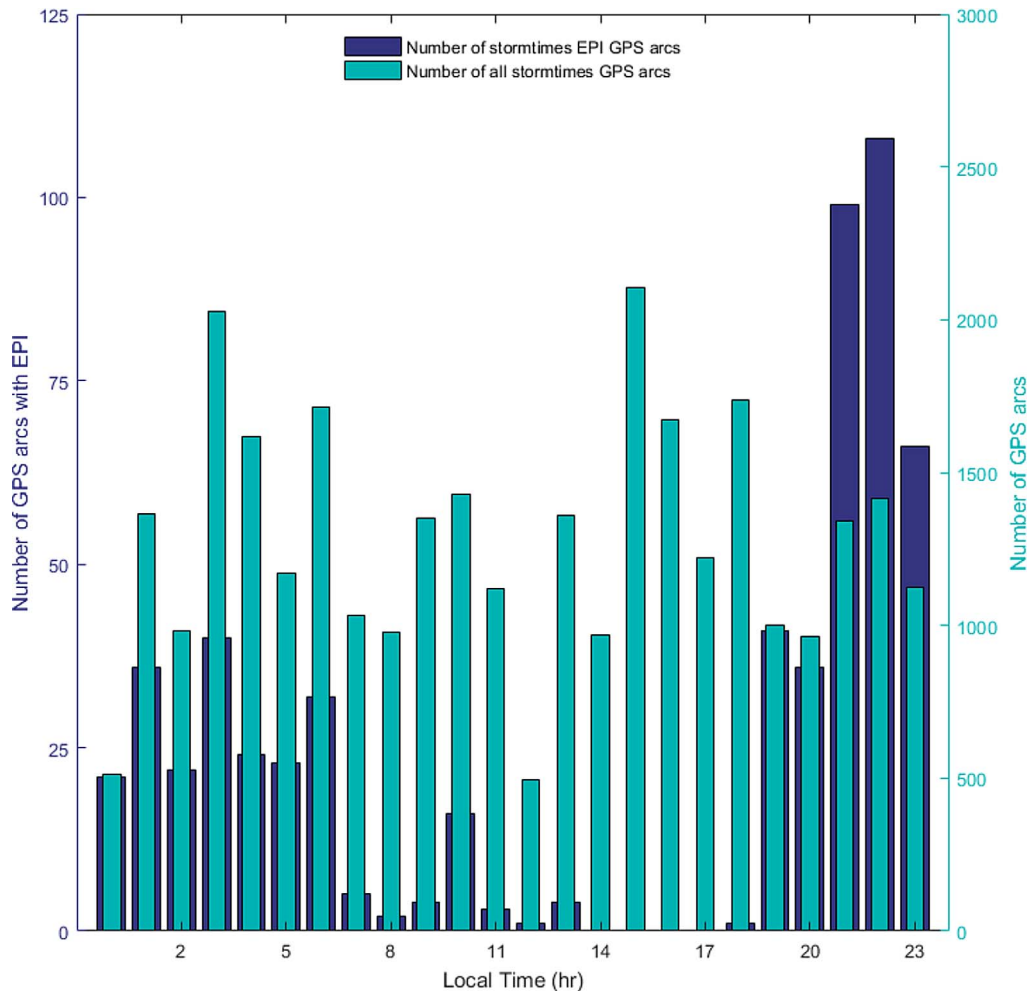


**Fig. 8.** The local time distributions of the numbers of total tracked GPS arcs (green) and the GPS arcs that observed EPIs (dark blue) during all the combined storm events. The storm time was considered from initial phase onset to the end of the recovery phase.

The algorithm was validated by visual inspections with corresponding in-situ electron density data for individual cases and a few examples are presented in Figures 1–4. It was further tested by statistics during quiet time between November 2014 and December 2015. The result as shown in Figure 5 agrees with previous studies (Zakharenkova et al., 2016; Wan et al., 2018; Aa et al., 2020; Park et al., 2021).

In this study, the relative occurrence of the storm time EPIs was found to be highest during the post-sunset/midnight (19:00–00:00 LT). This is consistent with previous studies (e.g. Wan et al., 2019) and it is understandable that the background condition of the ionosphere at this LT sector, which is prone to RTI makes it suitable to EPI occurrence under normal geomagnetic condition. More so, the superposition effect of the under-shielding PPEF on the existing post-sunset PRE provides the conditions required for the generation of EPIs during the early stages of the geomagnetic storms (Huang et al., 2001; Abdu, 2012; Sun et al., 2012).

On the other hand, after the subsidence of the PPEF and emergence of DDEF during the recovery phase, usually 4 h or more after the storm onset, it can be observed that the EPI activities got subsided at the post-sunset sector (Fig. 10f and g), while

at the same time the post-midnight EPIs got enhanced. The results in Figure 10g–q show that the effects of the storm time disturbance neutral wind can inhibit EPIs during the post-sunset several hours after the storm onset. It is also possible that there is the existence of an EPI suppressing force during the early hours of the initial phase of the geomagnetic storms as seen in Figure 10a and b, or possibly the majority of the storms had not yet commenced during these epochs.

The storm time EPIs were also quite pronounced during the post-midnight sector in Figure 8, a period during which the vertical ion drift velocity is usually downward. The occurrence of geomagnetic storm during this LT sector of the recovery phase has the potential of reversing the quiet time zonal electric fields from westward (responsible for the downward drift) to eastward direction so as to raise the  $F_2$ -layer to higher altitudes. The drivers capable of causing such reversal during storm times are the prompt penetration electric fields (PPEF) due to coupling between the ionosphere and magnetosphere and disturbance dynamo electric fields (DDEF) due to the Joule heating at the auroral latitudes leading to disturbance in the neutral wind patterns. The PPEF of the under-shielding (over-shielding) condition is westward (eastward) during the post-midnight LT.

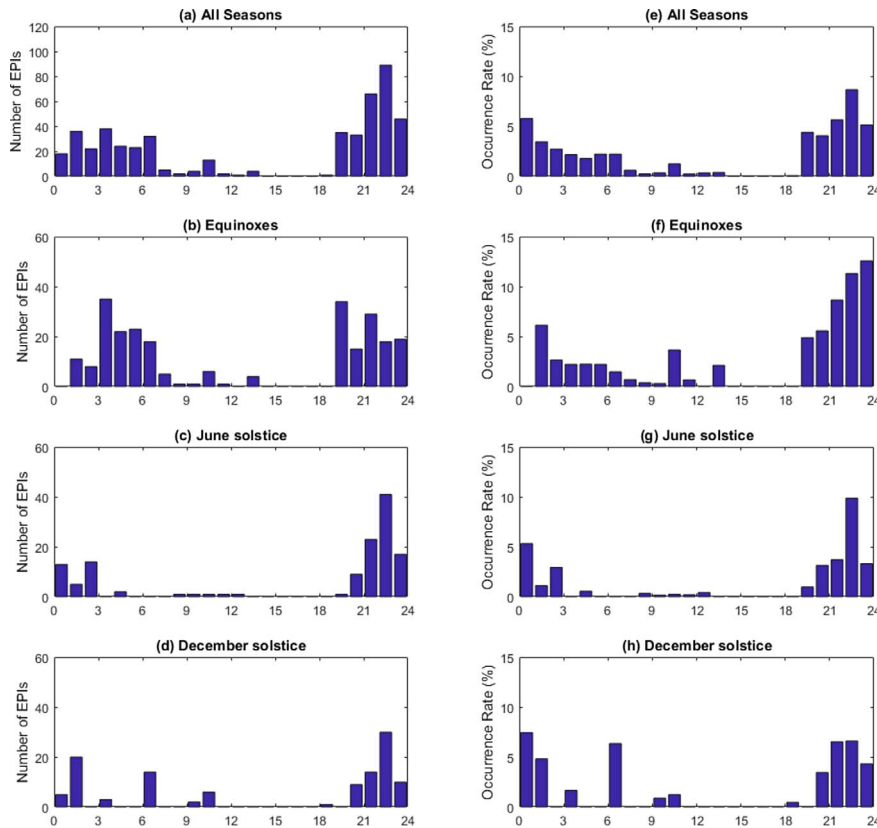


**Fig. 9.** (a)–(d) The local time distributions of the storm time numbers of EPIs (e)–(h) and the percentage occurrence rate for all seasons, equinoxes, June solstice and December solstice from the top to the bottommost panel, respectively, in this order. The storm time was considered from main phase onset to the end of the recovery phase.

Furthermore, during the post-midnight, the over-shielding PPEF and DDEF act eastward and are dominant during the recovery phase of geomagnetic storms, while the under-shielding PPEF has a westward direction and is dominant during the main phase. Hence, the over-shielding PPEF and DDEF played significant roles in the triggering of EPIs during the recovery phase of the geomagnetic storms in the post-midnight/pre-sunrise sector.

It was clearly observed from this study that during the post-sunset LTs EPIs appeared to be greatly enhanced during the first 6 h of the main phase onset (Fig. 10e), while the post-midnight/morning sector got significantly enhanced after about 6 h from the main phase onset (Fig. 10f). This is consistent with the results of Wan et al. (2019) who used ion density and meridional component of the vertical ion drift velocity from the Ionospheric Plasma and Electrodynamics Instrument onboard ROCSAT-1 in their study. They observed that the occurrence of irregularities at post-sunset/midnight got enhanced in a short while after the storm onset and the cause was attributed to the strengthening of PRE by PPEF. This was followed by a long-lasting suppression attributed to the weakening of PRE by DDEF.

Besides the PPEF and DDEF, another factor that can set up a suitable condition for the RTI during the post-midnight is the effect due to gravity waves traveling equatorward in the form of ionospheric disturbances, which emanate from substorm activities. These waves propagate in the neutrals and significantly

increase the ionic recombination rate on the bottom side of the  $F$ -layer (Davis, 1971; Bowmann, 1978). It steepens the density gradient at the bottom side and causes RTI to dominate during the recovery phase.

Furthermore, it should be noted that most of the irregularities observed during the main phase at the post-midnight sector in Figure 10e may be associated with a brief recovery in the ring current strength. When this happens, it can lead to the sudden incursion of over-shielding PPEF during the main phase and could raise the  $F_2$  peak height and possibly trigger ionospheric irregularities during the post-midnight sector.

Moreover, daytime irregularities have been observed in this study and more prominently during the early morning at the 2nd–4th epochs (recovery phase). Daytime irregularities had been previously observed under certain conditions, which made the daytime electron density similar to the nighttime condition (Burke, 1979; Li et al., 2010; Luo et al., 2020). Park et al. (2015) based on previous literature summarized the features of the daytime irregularities thus; (1) they are observed more frequently during the early morning than noon/late afternoon sector, (2) they generally occur at lower magnetic latitudes than nighttime EPIs (afternoon:  $\leq 20^\circ$  and nighttime:  $\leq 30^\circ$ ), (3) at high altitude, (4) and under disturbed geomagnetic conditions. All these points are consistent with the observed daytime EPIs under this study (see Figs. 4 and 10).

The observed irregularities during the daytime sector can be explained in light of the understanding that irregularities that are

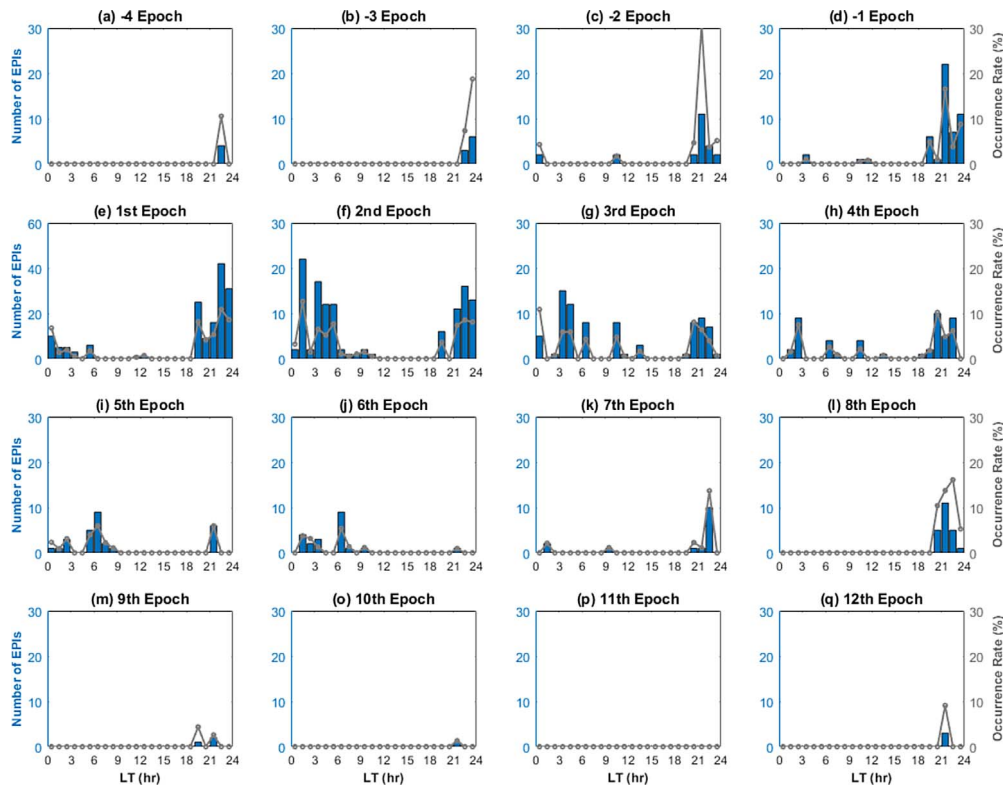


**Fig. 10.** The LT distribution of the numbers of EPIs (blue bars) and percentage occurrence rate (gray curves) during different epochs of the superposed storms. (a)–(d) and (e)–(q) show the epochs before and after the main phase onset (each epoch lasts for 6 h).

freshly initiated between post-sunset and pre-sunrise can persist till post-sunrise sector under the influence of DDEF and/or equatorward winds after the *E*-region conductivity recouples the *F*-region. Although the newly generated ionization at sunrise tends to submerge the persisted bubbles, it may take several hours for these bubbles to decay (Aarons & DasGupta, 1984). Tulasi Ram et al. (2015) reported the occurrence of fresh pre-sunrise field aligned irregularities (FAI) during the recovery phase of a minor storm. These FAIs persisted for more than 90 min into the morning sector and was associated with overshielding PPEF. On the other hand, Luo et al. (2020) attributed their observations of persisted irregularities emanating from the freshly initiated pre-sunrise irregularities about 3 h earlier to the effect of DDEF.

The daytime EPIs, which are fossil EPIs of the previous day's post-sunset/pre-sunrise EPIs thrive more at the topside as they are better protected from active dayside photo-ionization and refilling (Huang et al., 2013; Luo et al., 2020). Hence, it implies that the intense ionization condition during 14:00–17:00 LT may have completely submerged the persisted bubbles, accounting for the non-existence of EPI during this LT interval. However, Chau & Woodman (2001), had previously observed EPIs during 14:00–16:00 LT at the recovery phase of a moderate geomagnetic storm. EPIs cannot last so long in the daytime and it is more likely that the daytime condition of the ionosphere during the storm-time was similar to the nighttime.

In this study it was observed that the daytime EPIs in Figure 10 were more pronounced during the recovery phase of the storms most especially after about 18 h from the

1st epoch. It can be noticed that the period that the emergence of these daytime EPIs became significant during the recovery phase correlates with the long time duration after which the EPIs had been generated at the storm onset and are likely maintained by DDEF (Wan et al., 2019), and other possible geophysical factors.

## 5 Conclusion

In this study, the variations of topside ionospheric irregularities during intense geomagnetic storms in 2015 were examined. The main results are summarized as follows:

1. An algorithm was developed to detect significant ionospheric irregularities, and to avoid undesirable enhancements in ROTI that are not associated with plasma density irregularities. The algorithm has been validated by corresponding in situ electron density data of some individual cases and by statistics and the performance was efficient.
2. The intensity of the detected EPI was mainly controlled by the threshold set for the rate of TEC index (ROTI), that is  $\text{ROTI} \geq 0.75$  TECU/min. In addition, the number of peaks in  $|\text{ROTI}|$  during the interval of  $\text{ROTI} \geq 0.75$  TECU/min was used in eliminating the EIA, while the 25th and 75th inter-percentile range population and value of  $|\text{ROTI}|$  during the above interval were used to detect the presence of irregularities so as to discriminate TEC depletions from enhancements.

3. EPIs were observed during nighttime, but took place at daytime occasionally during the main phase of the storms in this study. Under this condition, the daytime electron density could be subjected to similar condition as at night time and can support the existence of irregularities.
4. It was also observed that the majority of the observed EPIs during the post-midnight sector of the recovery phase got significantly enhanced after 6 h from the main phase onset, while the post-sunset EPIs subsided, which indicates the effects of DDEF driver.

**Acknowledgements.** This work is supported by the National Science Foundation of China (41974181, 42188101), the Project of Stable Support for Youth Team in Basic Research Field, CAS (YSBR-018), the B-type Strategic Priority Program of the Chinese Academy of Sciences (XDB41000000), the fundamental research funds for the central universities, the pre-research project on Civil Aerospace Technologies No. D020105 funded by China's National Space Administration, and the Open Research Project of Large Research Infrastructures of CAS – “Study on the interaction between low/mid-latitude atmosphere and ionosphere based on the Chinese Meridian Project”. O. Jimoh was supported by the China Scholarship Council. J. Zhong was also supported by the National Natural Science Foundation of China (41804150). F. Huang was supported by the National Natural Science Foundation of China (42004136), the China Postdoctoral Science Foundation (2020T130628 and 2019M662170), the Fundamental Research Funds for the Central Universities (WK2080000130), and the Joint Open Fund of Mengcheng National Geophysical Observatory (No. MENGO-202010). We acknowledge the use of data from NASA (<ftp://podaac-ftp.jpl.nasa.gov/>) for the GRACE data, and ESA Earth Online service (<http://earth.esa.int/swarm/>) for the Swarm data. The editor thanks three anonymous reviewers for their assistance in evaluating this paper.

## References

- Aa E, Zou S, Liu S. 2020. Statistical analysis of equatorial plasma irregularities retrieved from Swarm 2013–2019 observations. *J Geophys Res Space Phys* **125**: e2019JA027022. <https://doi.org/10.1029/2019JA027022>.
- Aarons J, DasGupta A. 1984. Equatorial scintillations during the major magnetic storm of April 1981. *Radio Sci* **19**(3): 731–739. <https://doi.org/10.1029/RS019i003p00731>.
- Aarons J. 1991. The role of the ring current in the generation or inhibition of equatorial F layer irregularities during magnetic storms. *Radio Sci* **26**: 1131–1149. <https://doi.org/10.1029/91RS00473>.
- Abdu MA, Bittencourt JA, Batista IS. 1981. Magnetic declination control of the equatorial F region dynamo electric field development and spread F. *J Geophys Res* **86**: 11443–11446. <https://doi.org/10.1029/JA086iA13p11443>.
- Abdu MA. 1997. Major phenomena of the equatorial ionosphere–thermosphere system under disturbed conditions. *J Atmos Sol Terr Phys* **13**: 1505–1519.
- Abdu MA, Batista IS, Takahashi H, MacDougall J, Sobral JHA, Medeiros AF, Trivedi NB. 2003. Magnetospheric disturbance induced equatorial plasma bubble development and dynamics: A case study in Brazilian sector. *J Geophys Res* **108**: A12. <https://doi.org/10.1029/2002JA009721>.
- Abdu MA, Iyer KN, de Medeiros RT, Batista IS, Sobral JHA. 2006. Thermospheric meridional wind control of equatorial spread F and evening prereversal electric field. *Geophys Res Lett* **33**(L07106): 1–4.
- Abdu MA. 2012. Equatorial spread F/plasma bubble irregularities under storm time disturbance electric fields. *J Atmos Sol Terr Phys* **75**(76): 44–56.
- Abdu MA. 2016. Electrodynamics of ionospheric weather over low latitudes. *Geosci Lett* **3**(1): 11. <https://doi.org/10.1186/s40562-016-0043-6>.
- Abdu MA. 2019. Day-to-day and short-term variabilities in the equatorial plasma bubble/spread F irregularity seeding and development. *Prog Earth Planet Sci* **6**: 11. <https://doi.org/10.1186/s40645-019-0258-1>.
- Amaechi PO, Oyeyemi EO, Akala AO, Amory-Mazaudier C. 2020. Geomagnetic activity control of irregularities occurrences over the crests of the African EIA. *Earth Space Sci* **7**: e2020EA001183. <https://doi.org/10.1029/2020EA001183>.
- Basu B. 1997. Generalized Rayleigh–Taylor instability in the presence of time-dependent equilibrium. *J Geophys Res Space Phys* **102**(A8): 17305–17312. <https://doi.org/10.1029/97ja01239>.
- Basu S, et al. 2001. Ionospheric effects of major magnetic storms during the International Space Weather Period of September and October 1999: GPS observations, VHF/UHF scintillations, and in situ density structures at middle and equatorial latitudes. *J Geophys Res* **106**(A12): 30389–30413. <https://doi.org/10.1029/2001JA001116>.
- Blanc M, Richmond AD. 1980. The ionospheric disturbance dynamo. *J Geophys Res* **85**: 1669–1686.
- Blewitt G. 1990. An automatic editing algorithm for GPS data. *Geophys Res Lett* **17**(3): 199–202. <https://doi.org/10.1029/GL017i003p00199>.
- Bolaji OS, Adebisi SJ, Fashae JB. 2018. Characterization of ionospheric irregularities at different longitudes during quiet and disturbed geomagnetic conditions. *J Atmos Sol Terr Phys* **182**: 93–100. <https://doi.org/10.1016/j.jastp.2018.11.007>.
- Booker HG, Wells HW. 1938. Scattering of radio waves by the F-region of the ionosphere. *J Geophys Res* **43**(3): 249–256. <https://doi.org/10.1029/TE043i003p00249>.
- Bowmann GG. 1978. A relationship between polar magnetic substorms ionospheric height rises and the occurrence of Spread-F. *J Atmos Sol Terr Phys* **40**: 713–722. [https://doi.org/10.1016/0021-9169\(78\)90129-0](https://doi.org/10.1016/0021-9169(78)90129-0).
- Burke WJ. 1979. Plasma bubbles near the dawn terminator in the topside ionosphere. *Planet Space Sci* **27**: 1187–1193. [https://doi.org/10.1016/0032-0633\(79\)90138-7](https://doi.org/10.1016/0032-0633(79)90138-7).
- Burke WJ, Gentile LC, Huang CY, Valladares CE, Su SY. 2004. Longitudinal variability of equatorial plasma bubbles observed by DMSP and ROCSAT-1. *J Geophys Res* **109**: A12301. <https://doi.org/10.1029/2004JA010583>.
- Chau JL, Woodman RF. 2001. Interferometric and dual beam observations of daytime Spread-F-like irregularities over Jicar-marca. *Geophys Res Lett* **28**: 3581–3584. <https://doi.org/10.1029/2001GL013404>.
- Cherniak I, Zakharenkova I. 2016. High-latitude ionospheric irregularities: Differences between ground- and space-based GPS measurements during the 2015 St. Patrick's Day storm. *Earth Planets Space* **68**(1): 136. <https://doi.org/10.1186/s40623-016-0506-1>.
- Choi KR, Lightsey EG. 2008. Estimation of total electron content (TEC) using spaceborne GPS measurements. *J Astronaut Sci* **56**: 375–399. <https://doi.org/10.1007/BF03256559>.

- Davis MJ. 1971. On polar substorms as the source of large-scale traveling ionospheric disturbances. *J Geophys Res (1896-1977)* **76(19)**: 4525–4533. <https://doi.org/10.1029/JA076i019p04525>.
- Eccles JV, Maurice JPS, Schunk RW. 2015. Mechanisms underlying the prereversal enhancement of the vertical plasma drift in the low-latitude ionosphere. *J Geophys Res Space Phys* **120**: 4950–4970. <https://doi.org/10.1002/2014JA020664>.
- Farley DT, Bonelli E, Fejer BG, Larsen ME. 1986. The prereversal enhancement of the zonal electric field in the equatorial ionosphere. *J Geophys Res* **91**: 13723–13728.
- Fejer BG, Farley DT, Balsley BB, Woodman RF. 1976. Radar studies of anomalous velocity reversals in the equatorial ionosphere. *J Geophys Res* **81(25)**: 4621–4626. <https://doi.org/10.1029/JA081i025p04621>.
- Fejer BG, Scherliess L. 1995. Time-dependent response of equatorial ionospheric electric field to magnetospheric disturbances. *Geophys Res Lett* **22(7)**: 851–854. <https://doi.org/10.1029/95gl00390>.
- Fejer BG, Scherliess L. 1998. Mid- and low-latitude prompt-penetration ionospheric zonal plasma drifts. *Geophys Res Lett* **25(16)**: 3071–3074. <https://doi.org/10.1029/98gl02325>.
- Foelsche U, Kirchengast G. 2002. A simple “geometric” mapping function for the hydrostatic delay at radio frequencies and assessment of its performance. *Geophys Res Lett* **29(10)**: 111–114. <https://doi.org/10.1029/2001gl013744>.
- Friis-Christensen E, Lühr H, Hulot G. 2006. Swarm: A constellation to study the Earth’s magnetic field. *Earth Planets Space* **58**: 351–358.
- Greenspan ME, Rasmussen CE, Burke WJ, Abdu MA. 1991. Equatorial density depletions observed at 840 km during the great magnetic storm of March 1989. *J Geophys Res Space Phys* **96(A8)**: 13931–13942. <https://doi.org/10.1029/91ja01264>.
- Greenwald RA, Baker KB, Dudeney JR, Pinnock M, Jones TB, Thomas EC, et al. 1995. DARN/SuperDARN: A global view of the dynamics of high-latitude convection. *Space Sci Rev* **71(1–4)**: 761–796. <https://doi.org/10.1007/BF00751350>.
- Heelis RA, Kendall PC, Moffet RJ, Windle DW, Rishbeth H. 1974. Electrical coupling of the E- and F-regions and its effects on the F region drifts and winds. *Planet Space Sci* **22**: 743–756. [https://doi.org/10.1016/0032-0633\(74\)90144-5](https://doi.org/10.1016/0032-0633(74)90144-5).
- Huang CY, Burke WJ, Machuzak JS, Gentile LC, Sultan PJ. 2001. DMSP observations of equatorial plasma bubbles in the topside ionosphere near solar maximum. *J Geophys Res Space Phys* **106(A5)**: 8131–8142. <https://doi.org/10.1029/2000ja000319>.
- Huang CY, Burke WJ, Machuzak JS, Gentile LC, Sultan PJ. 2002. Equatorial plasma bubbles observed by DMSP satellites during a full solar cycle: Toward a global climatology. *J Geophys Res Space Phys* **107(A12)**: SIA 7-1–SIA 7-10. <https://doi.org/10.1029/2002ja009452>.
- Huang C-S, de La Beaujardiere O, Roddy PA, Hunton DE, Ballenthin JO, Hairston MR. 2013. Long-lasting daytime plasma bubbles observed by the C/NOFS satellite. *J Geophys Res Space Phys* **118**: 2398–2408.
- Huang C-S, de La Beaujardiere O, Roddy PA, Hunton DE, Liu JY, Chen SP. 2014. Occurrence probability and amplitude of equatorial ionospheric irregularities associated with plasma bubbles during low and moderate solar activities (2008–2012). *J Geophys Res Space Phys* **119**: 1186–1199. <https://doi.org/10.1002/2013JA019212>.
- Huang FQ, Lei JH, Xiong C, Zhong JH, Li GZ. 2021. Observations of equatorial plasma bubbles during the geomagnetic storm of October 2016. *Earth Planet Phys* **5(5)**: 1–10. <https://doi.org/10.26464/epp2021043>.
- Hysell DL, Burcham JD. 1998. JULIA radar studies of equatorial spread F. *J Geophys Res* **103(A12)**: 29155–29167. <https://doi.org/10.1029/98JA02655>.
- Hysell DL, Kudeki E. 2004. Collisional shear instability in the equatorial F region ionosphere. *J Geophys Res* **109**: A11301. <https://doi.org/10.1029/2004JA010636>.
- Jimoh O, Lei J, Zhong J, Owolabi C, Luan X, Dou X. 2019. Topside ionospheric conditions during the 7–8 September 2017 Geomagnetic storm. *J Geophys Res Space Phys* **124(11)**: 9381–9404. <https://doi.org/10.1029/2019ja026590>.
- Jin H, Zou S, Chen G, Yan C, Zhang S, Yang G. 2018. Formation and evolution of low-latitude F region field-aligned irregularities during the 7–8 September 2017 storm: Hainan coherent scatter phased array radar and digisonde observations. *Space Weather* **16**: 648–659. <https://doi.org/10.1029/2018SW001865>.
- Jin Y, Spicher A, Xiong C, Clausen LBN, Kervalishvili G, Stolle C, Miloch WJ. 2019. Ionospheric plasma irregularities characterized by the Swarm satellites: Statistics at high latitudes. *J Geophys Res Space Phys* **124**: 1262–1282. <https://doi.org/10.1029/2018JA026063>.
- Kelley MC. 2009. *The Earth’s ionosphere plasma physics and electrodynamics*, 2nd edn. Academic Press, San Diego, CA.
- Kikuchi T, Luehr H, Schlegel K, Tachihara H, Shinohara M, Kitamura TI. 2000. Penetration of auroral electric fields to the equator during a substorm. *J Geophys Res* **105**: 23251–23261. <https://doi.org/10.1186/s40562-016-0035-6>.
- Kil H, Heelis RA. 1998. Global distribution of density irregularities in the equatorial ionosphere. *J Geophys Res* **103(A1)**: 407–417.
- Kumar S, Chen W, Liu Z, Ji S. 2016. Effects of solar and geomagnetic activity on the occurrence of equatorial plasma bubbles over Hong Kong. *J Geophys Res Space Phys* **121**: 9164–9178. <https://doi.org/10.1002/2016JA022873>.
- Lei J, Wang W, Burns AG, Yue X, Dou X, Luan X, Solomon SC, Liu YC-M. 2014. New aspects of the ionospheric response to the October 2003 superstorms from multiple-satellite observations. *J Geophys Res Space Phys* **119**: 2298–2317. <https://doi.org/10.1002/2013JA019575>.
- Li G, Ning B, Hu L, Liu L, Yue X, et al. 2010. Longitudinal development of low-latitude ionospheric irregularities during the geomagnetic storms of July 2004. *J Geophys Res* **115**: A04304. <https://doi.org/10.1029/2009JA014830>.
- Li G, Otsuka Y, Ning B, Abdu MA, Yamamoto M, Wan W, Liu L, Abadi P. 2016. Enhanced ionospheric plasma bubble generation in more active ITCZ. *Geophys Res Lett* **43**: 2389–2395. <https://doi.org/10.1002/2016GL068145>.
- Li G, Ning B, Abdu MA, Wang C, Otsuka Y, Wan W, Lei J, Nishioka M, Tsugawa T, Hu L, et al. 2018. Daytime F-region irregularity triggered by rocket-induced ionospheric hole over low latitude. *Prog Earth Planet Sci* **5**: 11.
- Li Q, Zhu Y, Fang K, Fang J. 2020. Statistical study of the seasonal variations of TEC depletion and the ROTI during 2013–2019 over Hong Kong. *Sensor* **20**: 6200. <https://doi.org/10.3390/s20216200>.
- Luo W, Xiong C, Xu J, Zhu Z, Chang S. 2020. The low-latitude plasma irregularities after sunrise from multiple observations in both hemispheres during the recovery phase of a storm. *Remote Sens* **12**: 2897. <https://doi.org/10.3390/rs12182897>.
- Makela JJ, Miller ES. 2008. Optical observations of the growth and day-to-day variability of equatorial plasma bubbles. *J Geophys Res* **113**: A03307. <https://doi.org/10.1029/2007JA012661>.
- Mannucci AJ, Wilson BD, Yuan DN, Ho CH, Lindqwister UJ, Runge TF. 1998. A global mapping technique for GPS-derived ionospheric total electron content measurements. *Radio Sci* **33(3)**: 565–582. <https://doi.org/10.1029/97rs02707>.
- Maruyama T. 1988. A diagnostic model for equatorial spread F, 1. Model description and application to electric field and neutral wind effects. *J Geophys Res* **93(A12)**: 14611–14622.

- McClure JP, Hanson WB, Hoffman JF. 1977. Plasma bubbles and irregularities in the equatorial J. equatorial ionosphere. *J Geophys Res* **82**: 2650.
- McClure JP, Singh S, Bamgboye DK, Johnson FS, Kil H. 1998. Occurrence of equatorial F region irregularities: Evidence for tropospheric seeding. *J Geophys Res* **103(A12)**: 29119–29135.
- Oladipo OA, Schüler T. 2013. Equatorial ionospheric irregularities using GPS TEC derived index. *J Atmos Sol Terr Phys* **92**: 78–82.
- Oya H, Takahashi T, Watanabe S. 1986. Observation of low latitude ionosphere by the impedance probe on board the Hinotori satellite. *J Geomag Geoelectr* **38**: 111–123.
- Park J, Stolle C, Xiong C, Lühr H, Pfaff RF, Buchert S, Martinis CR. 2015. A dayside plasma depletion observed at midlatitudes during quiet geomagnetic conditions. *Geophys Res Lett* **42**: 967–974. <https://doi.org/10.1002/2014GL062655>.
- Park J, Kil H, Stolle C, Lühr H, Coley WR, Coster A, Kwak YS. 2016. Daytime midlatitude plasma depletions observed by Swarm: Topside signatures of the rocket exhaust. *Geophys Res Lett* **43**: 1802–1809.
- Park J, Heelis R, Chao CK. 2021. Ion velocity and temperature variation around topside nighttime irregularities: Contrast between low and mid-latitude regions. *J Geophys Res Space Phys* **126**: e2020JA028810. <https://doi.org/10.1029/2020JA028810>.
- Pi X, Mannucci A, Lindqwister U, Ho C. 1997. Monitoring of global ionospheric irregularities using the worldwide GPS network. *Geophys Res Lett* **24(18)**: 2283–2286. <https://doi.org/10.1029/97GL02273>.
- Pradipta R, Valladares CE, Doherty PH. 2015. An effective TEC data detrending method for the study of equatorial plasma bubbles and traveling ionospheric disturbances. *J Geophys Res Space Phys* **120**: 11048–11055. <https://doi.org/10.1002/2015JA021723>.
- Richmond AD, Peymirat C, Roble RG. 2003. Long-lasting disturbances in the equatorial ionospheric electric field simulated with a coupled magnetosphere–ionosphere–thermosphere model. *J Geophys Res* **108(A3)**: 1118. <https://doi.org/10.1029/2002JA009758>.
- Rishbeth H. 1971. Polarization fields produced by winds in the equatorial F-region. *Planet Space Sci* **19**: 357–369. [https://doi.org/10.1016/0032-0633\(71\)90098-5](https://doi.org/10.1016/0032-0633(71)90098-5).
- Rottger J. 1981. Equatorial spread F by electric field and atmospheric gravity wave generated by thunderstorms. *J Atmos Terr Phys* **43**: 453. [https://doi.org/10.1016/0021-9169\(81\)90108-2](https://doi.org/10.1016/0021-9169(81)90108-2).
- Seemala GK, Valladares CE. 2011. Statistics of TEC depletions observed over the South American continent for the year 2008. *Radio Sci* **46**: RS5019. <https://doi.org/10.1029/2011RS004722>.
- Stolle C, Lühr H, Fejer BG. 2008. Relation between the occurrence rate of ESF and the equatorial vertical plasma drift velocity at sunset derived from global observations. *Ann Geophys* **26(12)**: 3979–3988. <https://doi.org/10.5194/angeo-26-3979-2008>.
- Stolle C, Lühr H, Rother M, Balasis G. 2006. Magnetic signatures of equatorial spread F as observed by the CHAMP satellite. *J Geophys Res* **111**: A02304. <https://doi.org/10.1029/2005JA011184>.
- Su S-Y, Chao CK, Liu CH. 2008. On monthly/seasonal/longitudinal variations of equatorial irregularity occurrences and their relationship with the postsunset vertical drift velocities. *J Geophys Res* **113**: A05307. <https://doi.org/10.1029/2007JA012809>.
- Su SY, Liu CH, Chao CK. 2018. Post-midnight equatorial irregularity distributions and vertical drift velocity variations during solstices. *Adv Space Res* **61(7)**: 1628–1635. <https://doi.org/10.1016/j.asr.2017.07.005>.
- Sultan PJ. 1996. Linear theory and modeling of the Rayleigh–Taylor instability leading to the occurrence of equatorial spread-F. *J Geophys Res Space Phys* **101(A12)**: 26875–26891. <https://doi.org/10.1029/96ja00682>.
- Sun YY, Liu JY, Lin CH. 2012. A statistical study of low latitude F region irregularities at Brazilian longitudinal sector response to geomagnetic storms during post-sunset hours in solar cycle 23. *J Geophys Res* **117**: A03333. <https://doi.org/10.1029/2011JA017419>.
- Tapley BD, Bettadpur S, Watkins M, Reigber C. 2004. The gravity recovery and climate experiment: Mission overview and early results. *Geophys Res Lett* **31**: L09607. <https://doi.org/10.1029/2004GL019920>.
- Tsunoda RT. 2010. On seeding equatorial spread F during solstices. *Geophys Res Lett* **37**: L05102. <https://doi.org/10.1029/2010GL042576>.
- Tulasi Ram S, Ajith KK, Yamamoto M, Otsuka Y, Yokoyama T, Niranjan K, Gurubaran S. 2015. Fresh and evolutionary-type field-aligned irregularities generated near sunrise terminator due to overshielding electric fields. *J Geophys Res Space Phys* **120**: 5922–5930.
- Walach M-T, Grocott A. 2019. SuperDARN observations during geomagnetic storms, geomagnetically active times, and enhanced solar wind driving. *J Geophys Res Space Phys* **124**: 5828–5847. <https://doi.org/10.1029/2019JA026816>.
- Wan X, Xiong C, Rodriguez-Zuluaga J, Kervalishvili GN, Stolle C, Wang H. 2018. Climatology of the occurrence rate and amplitudes of local time distinguished equatorial plasma depletions observed by Swarm satellite. *J Geophys Res Space Phys* **123**: 3014–3026. <https://doi.org/10.1002/2017JA025072>.
- Wan X, Xiong C, Wang H, Zhang K, Zheng Z, He Y, Yu L. 2019. A statistical study on the climatology of the equatorial plasma depletions occurrence at topside ionosphere during geomagnetic disturbed periods. *J Geophys Res Space Phys* **124**: <https://doi.org/10.1029/2019JA026926>.
- Watanabe S, Oya H. 1986. Occurrence characteristics of low latitude ionosphere irregularities observed by impedance probe on board the Hinotori satellite. *J Geomag Geoelectr* **38**: 111–123.
- Woodman RF, La Hoz C. 1976. Radar observations of F-region equatorial irregularities. *J Geophys Res* **81(31)**: 5447–5466. <https://doi.org/10.1029/JA081i031p05447>.
- Xiong C, Park J, Lühr H, Stolle C, Ma SY. 2010. Comparing plasma bubble occurrence rates at CHAMP and GRACE altitudes during high and low solar activity. *Ann Geophys* **28**: 1647–1658. <https://doi.org/10.5194/angeo-28-1647-2010>.
- Yizengaw E, Retterer J, Pacheco EE, Roddy P, Groves K, Caton R, Baki P. 2013. Postmidnight bubbles and scintillations in the quiet-time June solstice. *Geophys Res Lett* **40**: 5592–5597. <https://doi.org/10.1002/2013GL058307>.
- Yizengaw E, Groves KM. 2018. Longitudinal and seasonal variability of equatorial ionospheric irregularities and electrodynamics. *Space Weather* **16**: 946–968. <https://doi.org/10.1029/2018SW001980>.
- Yue X, Schreiner WS, Hunt DC, Rocken C, Kuo YH. 2011. Quantitative evaluation of the low Earth orbit satellite-based slant total electron content determination. *Space Weather* **9(9)**: S09001. <https://doi.org/10.1029/2011sw000687>.
- Zakharenkova I, Astafyeva E. 2015. Topside ionospheric irregularities as seen from multi-satellite observations. *J Geophys Res Space Phys* **120(1)**: 807–824. <https://doi.org/10.1002/2014ja020330>.
- Zakharenkova I, Astafyeva E, Cherniak I. 2015. Early morning irregularities detected with spaceborne GPS measurements in the topside ionosphere: A multi-satellite case study. *J Geophys Res Space Phys* **120(10)**: 8817–8834. <https://doi.org/10.1002/2015ja021447>.
- Zakharenkova I, Astafyeva E, Cherniak I. 2016. GPS and in situ Swarm observations of the equatorial plasma density irregularities in the topside ionosphere. *Earth Planets Space* **68(1)**: 120. <https://doi.org/10.1186/s40623-016-0490-5>.

- Zakharenkova I, Cherniak I. 2018. Underutilized spaceborne GPS observations for space weather monitoring. *Space Weather* **16**(4): 345–362. <https://doi.org/10.1002/2017sw001756>.
- Zhong J, Lei J, Dou X, Yue X. 2016a. Is the long-term variation of the estimated GPS differential code biases associated with ionospheric variability? *GPS Solut* **20**: 313–319. <https://doi.org/10.1007/S10291-015-0437-5>.
- Zhong J, Lei J, Yue X, Dou X. 2016b. Determination of differential code bias of GNSS receiver onboard low earth orbit satellite. *IEEE Trans Geosci Remote Sens* **54**(8): 4896–4905. <https://doi.org/10.1109/TGRS.2016.2552542>.
- Zhong J, Lei J, Dou X, Yue X. 2016c. Assessment of vertical TEC mapping functions for space-based GNSS observations. *GPS Solut* **20**: 353–362. <https://doi.org/10.1007/S10291-015-0444-6>.

**Cite this article as:** Jimoh O, Lei J, Huang F & Zhong J 2022. The study of topside ionospheric irregularities during geomagnetic storms in 2015. *J. Space Weather Space Clim.* **12**, 32. <https://doi.org/10.1051/swsc/2022028>.